Large eddy simulation of spray and combustion characteristics with realistic chemistry and high-order numerical scheme under diesel engine-like conditions

Lei Zhou[1], Kai Hong Luo [1,2], Wenjin Qin[3], Ming,Jia[3], Shi Jin Shuai[1,4]

[1]Center for Combustion Energy, Tsinghua University, Beijing 100084, China
[2] Department of Mechanical Engineering, University College London, Torrington Place, London WC1E 7JE, UK
[3] School of Energy and Power Engineering，Dalian University of Technology，Dalian，116024
[4]State Key Laboratory of Automotive Safety and Energy, Tsinghua University, Beijing 100084, China

Abstract: The accuracy of large eddy simulation (LES) for turbulent combustion depends on suitably implemented numerical schemes and chemical mechanisms. In the original KIVA3V code, finite difference schemes such as QSOU (full name) and PDC (full name) cannot achieve good results or even computational stability when using coarse grids due to large numerical diffusion. In this paper, the MUSCL (Monotone Upstream-centered Schemes for Conservation Laws) differencing scheme is implemented into KIVA3V–LES code to calculate the convective term. In the meantime, Lu's n-heptane reduced 58-species mechanisms [Lu, 2011] is used to calculate chemistry with a parallel algorithm. Finally, improved models for spray injection are also employed. With these improvements, the KIVA3V-LES code is renamed as KIVALES-CP (Chemistry with Parallel algorithm) in this study. The resulting code was used to study the gas-liquid two phase jet and combustion under various diesel engine-like conditions in a constant volume vessel. The results show that using the MUSCL scheme can accurately capture the spray shape and fuel vapor penetration using even a coarse grid, in comparison with the Sandia experimental data. Similarly good results are obtained for three single-component fuels, i-Octane (C_8H_{18}), n-Dodecanese ($C_{12}H_{26}$), and n-Hexadecane ($C_{16}H_{34}$) with very different physical properties. Meanwhile the improved methodology is able to accurately predict ignition delay and flame lift-off length (LOL) under different oxygen concentrations from 10% to 21% with ambient density increasing from 14.8 kg/m^3 to 30.0 kg/m^3 and ambient temperatures from 850 K to 1300 K in a constant volume combustion chamber. With increasing oxygen concentration, the ignition delay time and consequently the flame LOL decrease, as the flame moves upstream as expected. On the other hand, reduction in the ambient temperature from 1000 K to 900 K retards the auto-ignition time and moves the burning location downstream under different oxygen concentrations.

Key words: large eddy simulation, high-order numerical schemes, liquid spray, detailed chemical mechanisms

Introduction

Liquid spray and combustion processes in an engine are extremely complex. They consist of a vast range of scales, ranging from chemical scales to the Kolomogrov scale and up to the cylinder diameter. Computational fluid dynamics (CFD) plays an important role in deeply understanding fuel spray and combustion characteristics and is being extensively used to design flow, spray and

31 combustion systems. Recently, thanks to the rapid increase in available computing power, Large

32 Eddy Simulation (LES) has received increasing attention and become a very attractive tool for

33 simulating complex spray and combustion processes in realistic systems.

34   In numerical simulations, high-order schemes are less frequently applied to complex systems,

35 such as internal combustion (IC) engines，than to canonical configurations, such as channels. In a

36 recent review, Rutland [1] pointed out that schemes of higher than second-order are difficult to be

37 applied in IC engines due to the use of complex dynamic grids. However, high-order schemes can

38 provide high-fidelity simulation and capture flow characteristics within a larger range of physical

39 scales on a given grid. They also save computer memory and allow higher resolution simulations.

40 Some recent studies have started to address this problem. Hori et al. [2] added a third-order cubic

41 interpolated profile (CIP) scheme into KIVALES code and investigated spray features by using four

42 different convection schemes. The results showed that low-order solutions can unphysically enlarge

43 spray penetration, suppress vortex development and influence temperature distribution due to large

44 numerical errors. A widely used LES code AVBP developed by CERFACS (Centre Européen de

45 Recherche et de Formation Avancée en Calcul Scientifique) and IFP (Institut Français de Pétrole) also

46 has a third-order spatial scheme, which has been applied to engine simulations [3-5] .

47   The MUSCL (Monotone Upstream-centered Schemes for Conservation Laws) scheme is one of

48 the most popular finite difference schemes, which employs limiter techniques. The MUSCL series

49 contain the second-order central scheme, the second-order upwind scheme and the third-order

50 scheme or the Fromm scheme. In this study we have added the third-order upwind MUSCL scheme

51 into KIVALES code to calculate the convective term in place of usual second-order or even

52 first-order scheme.

53   Low temperature combustion (LTC) is a novel combustion concept for diesel engines that can

54 simultaneously reduce NOx and PM emissions using the exhaust gas recirculation (EGR) technique

55 [6-9]. Many recent studies have focused on this combustion mode. Researchers at Sandia National

56 Laboratories, for example, have conducted a lot of experiments investigating the liquid spray and

57 combustion process under different oxygen concentrations (equivalent to EGR) in a constant volume

58 combustion chamber. On their website [10] they provide high-fidelity measurement data such as

59 spray shape, liquid and vapor penetration length, mixture-faction, ignition delay, flame lift-off length

60 and soot emissions which form a comprehensive experimental database for spray and combustion

61 models. In this study the n-heptane experiment data with different EGR conditions and other ambient

62 conditions are used to validate the present spray and combustion models.

63   In order to understand the complex combustion process and obtain accurate temperature

64 distribution, ignition delay time and flame lift-off length (LoL), a sufficiently detailed chemical

65 mechanism is required. In the original KIVA3V code the eddy dissipation model is used, which does

66 not give any detailed information about the combustion process. Kong et al. [11] interfaced the

67 chemistry module of the CHEMKIN code with KIVA for simulation of homogeneous charge

68 compression ignition engine processes. Simulations with detailed chemical kinetic mechanisms,

69 however, will require huge computational resources. Thus some alternative methods were proposed

70 such as chemistry tabulation. In this paper we develop an efficient way of implementing detailed

71 chemical mechanisms in combination with parallel chemistry computation with MPI.

72   This paper presents a further development of the LES methodology by incorporating the

73 high-order MUSCL scheme and parallel computation of detailed chemistry. The improved code,

74 based on KIVA3D, is renamed as KIVALES-CP, and applied to simulate spray and combustion

75 processes in a constant volume combustion chamber. A wide range of engine-like conditions have

76 been simulated by varying the type of fuels, initial temperature, oxygen concentration and gas

density, as in the Sandia experiments. The three-dimensional numerical results show that the predicted flow velocity field, liquid spray structure and droplet distribution, ignition delay time and flame lift-off length are in good agreement with the Sandia experimental data.

2 Numerical Models

2.1 LES Equations

Applying the filtering operator to the conservation equations of mass, momentum, energy and species equations results in the following filtered equations for two-phase flows [12]:

Continuity Equation：
$$\frac{\partial \overline{\rho}}{\partial t} + \frac{\partial \overline{\rho}\widetilde{u}_j}{\partial x_j} = \overline{\dot{\rho}^s} \tag{1}$$

Momentum Equations：
$$\frac{\partial \overline{\rho}\widetilde{u}_i}{\partial t} + \frac{\partial}{\partial x_j}\left(\overline{\rho}\widetilde{u}_i\widetilde{u}_j - \overline{\tau}_{ij} - \tau_{ij}^{sgs}\right) = \overline{F_i^s} \tag{2}$$

Energy Equation：
$$\frac{\partial \overline{\rho}\widetilde{e}}{\partial t} + \frac{\partial \overline{\rho}\widetilde{u}_j\widetilde{e}}{\partial x_j} + \overline{p}\frac{\partial \widetilde{u}_j}{\partial x_j} + \frac{\partial h_j^{sgs}}{\partial x_j}$$
$$+ \frac{\partial \overline{q}_j}{\partial x_j} - \overline{\sigma_{ij}\frac{\partial \widetilde{u}_i}{\partial x_j}} - \Theta^{sgs} = \overline{\dot{Q}^s} + \overline{\dot{Q}^c} \tag{3}$$

Species Equations：
$$\frac{\partial \overline{\rho}\widetilde{Y}_m}{\partial t} + \frac{\partial}{\partial x_j}\left(\overline{\rho}\widetilde{Y}_m\widetilde{u}_j - \overline{\rho D_m \frac{\partial \widetilde{Y}_m}{\partial x_j}} + \Phi_{j,m}^{sgs}\right)$$
$$= \overline{\dot{\rho}_m^{\ s}} + \overline{\dot{\rho}_m^{\ c}} \tag{4}$$

where the filtered viscous stress tensor and the heat flux vector [where is the expression for the heat flux?] are approximated, respectively, as

$$\tau_{ij}^{sgs} = -2\overline{\rho}\upsilon_t\left(\widetilde{S}_{ij} - \frac{1}{3}\widetilde{S}_{kk}\delta_{ij}\right) + \frac{2}{3}\overline{\rho}k^{sgs}\delta_{ij}, \quad \overline{q}_j$$ is the filtered heat flux, $\overline{\dot{Q}^s}$ is the energy release per unit

time due to spray, $\overline{\dot{Q}^c}$ is the chemical source term, $\dot{\rho}_m^{\ s}$ and $\dot{\rho}_m^{\ c}$ represent the density variation due to spray and chemistry, respectively. k^{sgs} is obtained by solving the subgrid turbulent kinetic energy equation:

$$\frac{\partial \overline{\rho}k^{sgs}}{\partial t} + \frac{\partial \overline{\rho}\widetilde{u}k^{sgs}}{\partial x_j} = P^{sgs} - D^{sgs} + \frac{\partial}{\partial x_j}\left(\overline{\rho}\frac{\nu_t}{Pr_t}\frac{\partial k^{sgs}}{\partial x_j}\right) + \overline{\dot{W}^s} \tag{5}$$

Here, P^{sgs} and D^{sgs} represent subgrid kinetic energy production rate and dissipation rate, respectively.

97   The subgrid heat flux h_j^{sgs} and subgrid species mass flux $\Phi_{j,m}^{sgs}$ are closed by the gradient diffusion

98   assumption. Details of this model can be found in reference [12].

99   **2.2 The MUSCL method**

100   The MUSCL method was proposed by Van Leer in 1979 [13]. In order to descript this method a

101   one-dimensional scalar hyperbolic conservation law is given below:

102    $$\frac{\partial u}{\partial t}+\frac{\partial f(u)}{\partial x}=0, \quad (6)$$

103   where $f(u)$ represents a flux variable.

104   Based on a semi-discrete conservative scheme the above equation can be defined as follows:

105    $$\frac{\partial u_j}{\partial t}+\frac{1}{h}\left(\hat{f}_{j+1/2}-\hat{f}_{j-1/2}\right)=0 \quad (7)$$

106   where h is calculate by $h=x_{j+1}-x_j$, and $x_{j+1/2}=x_j+h/2$.

107   Through splitting the flux the MUSCL formulation can obtain different semi-discrete schemes,

108   such as the second-order central scheme, and the second-order or third-order upwind scheme.

109   Different schemes, which depend on the expression of $\hat{u}_{j+1/2,L}$ and $\hat{u}_{j+1/2,R}$, can be written in a

110   unified form:

111    $$\hat{f}_{j+1/2}=f^+(\hat{u}_{j+1/2,L})+f^-(\hat{u}_{j+1/2,R}) \quad (8)$$

112   A more detailed form is

113    $$\hat{u}_{j+1/2,L}=u_j+\frac{1}{4}[(1-k)\overline{\delta}_x^-+(1+k)\overline{\delta}_x^+]u_j \quad (9)$$

114    $$\hat{u}_{j+1/2,R}=u_{j+1}-\frac{1}{4}[(1-k)\overline{\delta}_x^++(1+k)\overline{\delta}_x^-]u_{j+1} \quad (10)$$

115   In the above equation, if the upwind direction is left of cell j, then $\hat{f}_{j+1/2}=f^+(\hat{u}_{j+1/2,L})$; otherwise

116    $\hat{f}_{j+1/2}=f^-(\hat{u}_{j+1/2,R})$, $\overline{\delta}_x^+u_j=\min\text{mod}(\delta_x^+u_j,2\delta_x^-u_j)$ and $\overline{\delta}_x^-u_j=\min\text{mod}(\delta_x^-u_j,2\delta_x^+u_j)$. k is a factor [a

117   constant?]. In this study, we use k=1/3. If there schemes are used simply, they will produce

118   numerical oscillations. [How should the schemes be used without producing numerical oscillations?]

119   **2.3 Eulerian-Lagrangian Momentum Coupling**

120   The interaction between the Lagrangian (liquid) and the Eulerian (gas) phases is a very complex

121   process especially in turbulent flow, which determines the fuel/air mixture formation. The two-phase

122   coupling involves two aspects, "gas-to-liquid" and "liquid-to-gas" effects. In the "gas-to-liquid"

123   coupling, the change of the droplet velocity in the computation domain is determined by the drag

124   force $F_{i,d}$ acting on the droplet, which is calculated by the relative velocity between the liquid drop

125   and the gas, as follow:

126    $$dv_{d,i}/dt = F_{i,d}/m_d = 0.375\left(\rho/\rho_l\right)\left|V_{rel}\right|/r_d\,V_{rel}C_D, \quad (11)$$

127   where $m_d = 4/3\pi\rho_l r_d^3$ is the droplet mass. V_{rel} is the relative velocity between the liquid droplet and

128   the gas, ρ_l and r_d are the liquid droplet density and radius, respectively. C_D is the droplet drag

129   coefficient, computed as follows:

130    $$C_D = \begin{cases} \dfrac{24}{Re_d}(1+1/6\,Re_d^{2/3})\,Re_d < 1000 \\[2mm] 0.424 \qquad Re_d > 1000 \end{cases} \quad (12)$$

131   where Re_d is the droplet Reynolds number.

132   The relative velocity V_{rel} is a very important parameter and is calculated by gas velocity at the parcel

133   [you need to explain a parcel.] positions $\tilde{u}_i$, turbulent dispersion velocity $u'_{p,i}$ (when considering

134   turbulent effect on droplet)and droplet velocity $v_{d,i}$. The resulting formulation is $V_{rel} = \tilde{u}_i + u'_{p,i} - v_{d,i}$.

135   In order to accurately simulate the gas phase effect on the liquid phase, the velocity interpolation

136   model proposed by Nordin [14] was used, which employs an inverse distance weighting method

137   based on the 8 vertices of the cell at the parcel location. More details can be found in reference [14].

138   The dispersion velocity $u'_{p,i}$ is randomly chosen from a Gaussian distribution with standard

139   deviation $\sqrt{2/3k^{sgs}}$. k^{sgs} is the subgrid turbulent kinetic energy of the gas in the computational

140   cell in which the droplet is located. The Gaussian distribution at sub-grid scale is given by

141    $$G\left(u'_{p,i}\right) = \left(4/3\pi k^{sgs}\right)^{-3/2}\exp\left(-3u'^2_{p,i}/4k^{sgs}\right).$$

142   In the "liquid-to-gas" coupling, the effect of liquid motion on gas phase is treated as the

143   Lagrangian source terms of the Eulerian momentum equations of N-S Equations, $\overline{F_i^s}$ in Section 2.1.

144   The momentum source $\overline{F_i^s}$ is calculated by summing the rate of change of momentum of all droplets

145   in space and time. The expression is simply presented here for each computation cell:

146    $$\overline{F_i^s} = \sum_{per(i,j,k)} N_p \frac{4}{3}\pi\rho_l \left[\left(r^{n+1}\right)^3 v_d^{n+1} - \left(r^n\right)^3 v_d^n \right] \quad (13)$$

147   **2.4 Spray source term model**

148   In the sub-grid one equation turbulent kinetic energy equation (K-equation model), the spray

149   source term $\overline{\dot{W}^s}$ is defined as [15]: $\overline{\dot{W}^s} \equiv -F_i u_i'$, where u_i' is the subgrid gas velocity and

150    $F_i = \left(\sum_d F_{i,d}\right)\Big/ V_{cell}$ is the aerodynamic drag force.

151   In this study, the definition of the subgrid gas velocity is $u_i' \equiv u_i - \tilde{u}_i$.

152   where u_i and $\tilde{u}_i$ are the instantaneous and filtered velocities respectively.

153   So the spray source term can be expressed as $\overline{\dot{W}^s} \equiv -\left(\sum_d F_{i,d} u_i'\right)\Big/ V_{cell}$

154   In order to obtain the instantaneous velocity, an approximate deconvolution method (ADM) is

155   employed [15]. With successive filtering, ADM leads to the following expression for the

156   instantaneous velocity:

157    $$u_i \approx 3\tilde{u}_i - 3\tilde{\tilde{u}}_i + \tilde{\tilde{\tilde{u}}}_i \quad (14)$$

158   Accordingly, the subgrid gas velocity can be written simply as $u_i' = 2\tilde{u}_i - 3\tilde{\tilde{u}}_i + \tilde{\tilde{\tilde{u}}}_i$. Thus the final

159   form of the spray source term can be written as $\overline{\dot{W}^s} = -\frac{3}{8}\frac{C_D}{V_{cell}} \sum_d \{ \frac{m_d \rho V_{rel}}{r_d \rho_l}\left(\tilde{u}_i + u_{p,i}' - v_{d,i}\right)\left(2\tilde{u}_i - 3\tilde{\tilde{u}}_i + \tilde{\tilde{\tilde{u}}}_i\right)\} \cdot$

160   (15)

161   A more detailed derivation of the spray source term can be found in the reference [15].

162   **2.5 Spray breakup model**

163   The breakup of a liquid fuel jet is a very complex physical phenomenon which is influenced by the

164   aerodynamic liquid-gas interaction, the physical and thermal properties of the fuel and the ambient

165   environment. In the present study, the Kelvin-Helmholtz and Rayleigh-Taylor (KH-RT) model [16] is

166   used to predict the primary and subsequent secondary droplet breakup. In our previous study [???],

167   we analyzed the effects of the different breakup models on the atomization and evaporation of liquid

168   spray. The results show that the KH-RT is a good choice for liquid spray in large eddy simulation.

169   **2.6 Combustion computation**

170   In order to simulate the combustion process, parallel computation of detailed chemistry using the

171   Message-Passing Interface (MPI) has been implemented into KIVALES to form a new code

172   KIVALES-CP.. MPI allows for chemistry to be computed in parallel on multiple CPUs while the

173   fluid dynamics is still simulated on a single processor. This process is accomplished at each

174   computational time step. During the initial computation, CHEMKIN gas-phase library subroutines

175   are called to read species information into KIVALES and to update the species parameters and

176   calculate enthalpies . Once combustion occurs and chemical kinetic calculations start, KIVALES

177   transfers information on the temperature, pressure and compositions of each cell to CHEMKIN,

178   where chemical reactions are computed on a number of CPUs using decomposed uniform grids .

179   This parallel process can be completed because that the information is local and each of the

180   computational processors only needs to exchange information with its own group of cells [18]. At the

181   last stage, the heat release and new species compositions are returned to KIVALES and the entire

182   combustion computation cycle is completed.

183   The KIVALES-CP combustion model was used to calculate the heat release rate and change

184   species density as follows [17]

185 $$\overline{\dot{Q}^c} = -\sum_{m=1}^{M} \overline{\dot{w}_m} \Delta h_{f,m} W_m , \quad \overline{\dot{\rho}_m^c} = \overline{\dot{w}_m} W_m , m = 1, \cdots M \quad (16)$$

186 where $\overline{\dot{Q}^c}$ is heat released due to chemical reactions, $\Delta h_{f,m}$ is heat of formation of species m,

187 $\overline{\dot{w}_m}$ and W_m are molar production rate and molecular weight of species m, $\overline{\dot{\rho}_m^c}$ is density of

188 species m and M is total number of species, respectively.

189 Taking into consideration the turbulent kinetic energy effect, the molar production rate is

190 expressed as [11]:

191 $$\overline{\dot{w}_m} = \frac{\overline{Y_m^*} - \overline{Y_m}}{\tau_{lam} + \chi \tau_{turb}} , \quad (17)$$

192 where $\overline{Y_m^*}$ is equilibrium concentration, $\overline{Y_m}$ is current concentration, τ_{lam} is a kinetic timescale

193 $\tau_{lam} = (-Y_{fuel}^n / (Y_{fuel}^{n'} - Y_{fuel}^n))$, χ is the progress variable with a value ranging from 0 to 1 and

194 calculated by $\chi = (1 - e^{-r})/0.632$, r is the ratio of the amount of products to that of total reactive

195 species. τ_{turb} is a turbulent timescale. The final species concentration Y_i^{n+1} is calculated using the

196 following equation [11]:

197 $$Y_i^{n+1} - Y_i^n = \frac{\tau_{lam}}{\tau_{lam} + \chi \tau_{turb}} (Y_i^{n'} - Y_i^n) , \quad (18)$$

198 where, n+1 represents the new time, n represents the old time. Y_i^n and $Y_i^{n'}$ are the species

199 concentrations before and after the CHEMKIN model is called.

200 The turbulent timescale in the original model for RANS was based on the eddy turnover time

201 (k/ε). The new eddy characteristic time model for LES [19] is estimated by considering the

202 Kolmogorov scale as below:

203 $$\tau_{turb} = \left(\frac{\nu}{2\nu_t \overline{S_{ij} S_{ij}}} \right)^{0.5} , \text{ where } S_{ij} \text{ is the rate of strain tensor for the resolved scale.}$$

204 **3. Numerical Conditions**

205   In this study, the third-order MUSCL differencing scheme is employed to calculate the

206   convection terms in LES. The Lagrangian dispersed-phase approach is used to describe the liquid

207   phase. For spray modeling, the collision and coalescence model of O'Rourke is deployed. The

208   atomization model is the KH-RT model [16]. No-slip wall boundary conditions are applied to all

209   solid walls. The fully three-dimensional (3D) simulations were conducted in a cylindrical domain of

210   30 mm in diameter and 100 mm in height, as the base grid based on the studies of Bharadwaj et al.

211   [15], Hori et al. [2] and Zhou et al. [20]. The overall computational grid has about 800,000 cells with

212   the time step ranging from $1.*10^{-8}$ s to $1.*10^{-6}$ s. Table 1 shows the main experimental conditions by

213   Lyle et al. [21,22]. All the results are obtained with the same models and model parameters. For the

214   numerical calculation of combustion cases the massively parallel supercomputer in the Tsinghua

215   High-Performance Computing Center is employed. For a typical case, 12 processors (Intel Xenon

216   X5670 with 2.93GHz and 12MB cache) are used and run for about ten days.

217   **4. Results and Discussion**

218   **4.1 Code validation in an engine assembly**

219   In order to validate the MUSCL scheme in the new code KIVALES-CP, an axisymmetric

220   piston-cylinder assembly of Morse et al. [23] with a fixed central valve, shown in Fig.1, was

221   simulated in this work. The piston engine has a 150 mm bore, 60 mm stroke, and a 30 mm clearance

222   height. The piston is driven in a simple harmonic motion at a speed of 200 rpm (the mean piston

223   speed is 0.4m/s). For the engine configuration in Fig. 1, an overall computation mesh of 660,000

224   nodes is used. The mesh independence test was conducted in our previous work [24].

225   Fig.2a) presents the radial profiles of the axial mean velocity at crank angle of 36^0 and at

226   locations of 8, 7 and 6 cm from the cylinder bottom using the QSOU and MUSCL schemes. For

227 Morse's engine, Laser-Doppler anemometry has been used to obtain radial profiles of axial mean

228 velocity at different positions and crank angles. The mean velocity at a radius in each plane is

229 obtained by averaging 20 points at the same radius in the azimuthal direction.   In order to avoid the

230 influence of the first cycle, Fig.2 a) shows the second cycle results. From the velocity distributions at

231 three positions, it is clear that the axial mean velocity predictions using the MUSCL scheme are in a

232 much better agreement with the experimental data than results from the QSOU scheme. In particular,

233 the MUSCL scheme accurately predicted the peak value of the axial mean velocity at the axial plane

234 of 7 cm while the QSOU scheme completely missed this peak. The different performances of the two

235 schemes are because the third-order MUSCL scheme can reduce numerical diffusion in the

236 discretization of the momentum equation and predict the velocity distribution more accurately than

237 QSOU.

238   Fig.2 b) and c) present the radial profiles of the axial mean velocity at crank angle of 144^0 at

239 axial locations of 8, 7 ,6, 5 and 4 cm from the cylinder bottom using the QSOU and MUSCL

240 schemes. The MUSCL scheme gives better results at all positions except at 7 cm. Fig.2 b) and c) also

241 show the cycle-to-cycle variation (CCV), which is difficult for RANS to obtain. For the results using

242 the QSOU scheme it can be seen that the first-cycle results are very different from the results in the

243 second and third cycles, indicating slow convergence of the numerical solution.

244   Overall, the above results indicate that the MUSCL scheme used in KIVALES-CP has the

245 capability to capture accurately the spatial variations of in-cylinder velocities under engine-like

246 conditions.

247 **4.2 Spray simulation**

248 The high-order difference scheme MUSCL is further validated in the spray simulation. A dense grid

249 (about 6 million cells, cell size 0.25 mm) and a base grid (about 800,000 cells, cell size 0.5 mm) are

250   used. The QSOU scheme is tested on both grids while the MUSCL scheme is only used with the base

251   grid. In the simulations, liquid penetration length is defined as the axial location which has

252   accumulated 95% of injected fuel mass. Vapor penetration at any time is determined from the farthest

253   downstream location of 0.1% fuel mass fraction. Figure 3 a) shows predicted and measured liquid

254   spray and fuel vapor penetration with the MUSCL and QSOU schemes at an ambient temperature of

255   900 K for Case 1. [where is Case 1 defined?] Liquid penetration initially increases with time and

256   then stabilizes at a quasi-steady value after about 0.1 ms after start of injection (ASOI) for all three

257   cases. Compared to the experiment data, the liquid penetrations using the MUSCL scheme and

258   QSOU scheme with the base grid have the same results, which are slightly lower than experiment

259   data and results using the QSOU scheme with the dense grid. On the other hand, the vapor

260   penetration predictions have significant differences among the two schemes even on the same base

261   grid, especially at the later stage of spray. It can be seen that using the MUSCL scheme can predict a

262   much more accurate result than the QSOU scheme on the base grid, which is in good agreement with

263   experiment data and results using the QSOU scheme on a dense grid. Fig. 3 b) shows that using the

264   MUSCL scheme with the base grid and the QSOU scheme with the dense grid can well describe the

265   complex spray structure including the spray penetration length and vapour mixture fraction. As for

266   the results of QSOU with the base grid the unsteady turbulence behavior and diffusion are

267   suppressed. In contrast, using the MUSCL scheme gives close agreement with the Sandia data due to

268   decreased numerical diffusion and thus more accurate flow momentum. In terms of computational

269   cost for Case 1, the QSOU with the base grid needs 7 hours of simulation time, the MUSCL with the

270   base grid 8 hours, and the QSOU with dense grid 72 hours on one processor, as listed in Table 2.

271   The gas-liquid flow is a very complex phenomenon and in order to identify the liquid spray

272   structures more clearly, the Q criterion [25] was used in the present work. In the Q criterion, the

273   positive second invariant of the velocity gradient tensor (∇v) is used to describe the turbulent vortex

274   structure. A large and positive Q value implies a strong vortex region. The second invariant Q can be

275   written as $Q = \frac{1}{2}\left(\|\Omega\|^2 - \|S\|^2\right)$, where S and Ω are the symmetric and anti-symmetric components

276   of ∇v defined as $S = \frac{1}{2}\left(\nabla v + (\nabla v)^t\right)$ and $\Omega = \frac{1}{2}\left(\nabla v - (\nabla v)^t\right)$ respectively.

277   Figure 4 presents the influence of the convective schemes on the evolution of vortex with

278   injection time at 1.5ms ASOI for Case 1. It can be seen from Fig.4 that small eddy structures are

279   shown with the increase of Q value and strong eddies can be captured by the present models. It is

280   noted that unlike QSOU with the base grid, using MUSCL with the base grid can distinguish more

281   small eddies and capture strong vortex regions, even at the Q value of $4.5*10^8$. Thus in this study, the

282   MUSCL with the base grid is adopted to capture sufficiently detailed flow structures at a relatively

283   low computational cost.

284   In order to validate the MUSCL scheme further, the three single-component fuels, i-Octane

285   (C8H18), n-Dodecanese (C12H26), and n-Hexadecane (C16H34) are simulated, which have

286   different boiling points and liquid densities. The three types of fuels are selected to represent low

287   boiling point, medium boiling point and high boiling point fuel, respectively. Figure 5 shows

288   predicted results using LES with MUSCL and QSOU,[I cannot see any results using QSOU!]

289   compared with experimental images obtained by Mie-scattered light and shadowgraph method at the

290   end of injection of 1.82ms ASOI for case 2 [26]. For the simulation results, the black dots represent

291   liquid phase, while the bright area in experimental image means the liquid phase area. It can be seen

292   from the comparison in Fig.5 that predicted liquid penetration lengths with MUSCL are similar to the

293   experiment results and obviously better than the results of QSOU. The QSOU fails to predict the

294   change of liquid penetration length against liquid density. Note that decrease in the carbon number in

295   a fuel can result in reduction in the penetration length of liquid phase, owing to decrease in boiling

296 point and liquid density and promotion of evaporation at the same ambient temperature. The

297 decrease in the carbon number also can lower the molecular weight, liquid density and boiling

298 temperature, and decrease fuel vapor concentration in each cell. Thus for C8H18, it is easy to

299 evaporate and has enough time to diffuse in space, unlike fuel C16H34. The experiment in Fig.5 also

300 demonstrates this phenomenon. Quantitative results of liquid phase length for different liquid density

301 are presented in Fig.6. It can be seen that predicted results with MUSCL are in excellent agreement

302 with experimental data and have similar trends with increasing liquid density, although the

303 agreement for fuel C16H34 is not perfect. The QSOU scheme, on the other hand, has consistently

304 overpredicted the liquid phase length. Overall, the present MUSCL scheme can predict liquid spray

305 characteristics accurately under different fuel boiling points and liquid densities.

306 **4.3 Reaction case**

307 Chemistry is an essential factor influencing the ignition process. In order to simulate the

308 heptane spray and combustion process, seven chemistry mechanisms used frequently in internal

309 combustion engine are firstly investigated in terms of the auto-ignition delay time at two oxygen

310 concentrations in a constant volume vessel. The low oxygen concentration cases represent exhaust

311 gas recirculation (EGR) conditions. The detailed results are listed in Table 3. From the results it can

312 be seen that for 21% oxygen concentration, all the chemical mechanisms except Ra's give a

313 reasonable prediction of the auto-ignition delay time in comparison with the experiment data.

314 However, for the 12% oxygen concentration condition the auto-ignition delay time predicted by only

315 LU-88 and LU-55 chemical mechanisms is consistent with the experiment data. Note that the two

316 accurate mechanisms are derived from a two-stage directed relation graph (DRG) [27] starting from

317 the detailed LLNL mechanism with 561 species and 2539 elementary reactions [28]. Thus, the

318   LU-55 mechanism is chosen to simulate the combustion process under different oxygen

319   concentrations, ambient densities and ambient temperatures.

320   In this section, the flame lift-off length (LoL) and ignition delay time are predicted and discussed

321   using KIVALES-CP with the MUSCL scheme and Lu's n-heptane reduced 58-species mechanism

322   under different oxygen concentrations (EGR ratios), ambient temperatures and ambient gas densities.

323   These conditions are of relevance to the low temperature combustion (LTC) strategy for HCCI

324   engines. Note that this mechanism needs to invoke a mechanism-specific subroutine CKWYP to

325   compute the species production rates including quasi steady state (QSS) species. Figure 7 shows the

326   temperature and OH radical distributions at 2.0ms ASOI compared with Sandia experimental images.

327   In the experimental images, the red color field represents the high temperature region. In the

328   predicted results, the black color indicates the liquid phase while the white dash-dot line represents

329   the flame lift-off position. It can be seen that the temperature in the reaction zones generally

330   increases with increasing oxygen concentration (that is, less EGR). Note that, for oxygen

331   concentration of 10% the chamber temperature is very low and the burning is barely visible.

332   Simultaneously the OH radical concentration also increases with increasing oxygen concentration, as

333   chemical reactions become more intense. And the distributions of high OH radical concentrations are

334   consistent with the high temperature zones.

335   Figure 8 quantitatively predicts the effect of the oxygen concentrations on ignition delay time and

336   flame lift-off length (LO) using the present models in KIVALES-CP in comparison with measured

337   data under ambient initial temperatures of 900 K and 1000 K. As the size of the LES domain is

338   different from the experiment setup, so following the practice in [5] the ignition delay time in the

339   simulations is defined as the point in time when the temperature in the domain reaches half of the

340   peak temperature in the entire combustion process in the domain. The lift-off length is also defined

341   as the location where the temperature reaches half of the peak temperature in the entire combustion

342   process in the domain. With increasing oxygen concentration, the ignition delay time and

343   consequently the flame LOL decrease, as the flame moves upstream as expected. On the other hand,

344   when the ambient temperature is decreased from 1000 K to 900 K, the auto-ignition time is retarded

345   and the burning location is moved downstream under different oxygen concentrations. In fact, for the

346   ambient temperature of 900 K and oxygen concentration of 10% case, the combustion temperature is

347   so low that it is not easy to capture accurately the combustion characteristics and consequently there

348   is a considerable deviation from the Sandia data. Overall, the trends of ignition delay time and LOL

349   variation against the ambient temperature and oxygen concentration obtained by the improved LES

350   are consistent with the Sandia experimental data. Note that, comparing Fig. 7 and Fig. 8, the

351   definition of flame LOL using the half-temperature method in the work is the same as that of using

352   OH radical distribution method.

353   Ignition and flame location are heavily dependent on the mixture formation. The present LES

354   method with the MUSCL scheme can capture the vapor distribution more accurately as shown in

355   section 4.3. Thus, on the whole the temperature field variations with oxygen concentration are

356   accurately predicted by the present method compared with Sandia images. An interesting

357   phenomenon in LTC that decreasing oxygen concentration or increasing EGR can effectively retard

358   burning and decrease combustion temperature can also be obtained by the KIVALES-PC code with

359   the MUSCL scheme and Lu's n-heptane reduced 58-species mechanism.

360   Figure 9 presents the effect of the oxygen concentration on ignition delay time under ambient

361   density of 30.0 kg/m^3. The same trend of ignition delay time variation with an increase in the oxygen

362   concentration is obtained, as compared with that under ambient density of 14.8 kg/m^3. At oxygen

363   concentrations of 8% and 10% the computed ignition delay time is lower than the experiment data.

364 This may be due to the fact that the combustion temperature is so low under these conditions that

365 there are larger errors in the ignition delay time determined by both the simulation and experimental

366 data. In Fig.10 it can be seen that increasing ambient density causes the flame to move upstream

367 under the same ambient temperature of 1000 K and oxygen concentration of 15%. Combined with

368 Fig.8 and Fig.9, it is clear that an ambient density increase from 14.8 kg/m^3 to 30.0 kg/m^3 leads to a

369 decrease in flame LOL from 27 mm to 11 mm and in ignition delay time from 0.75 ms to 0.38 ms.

370 This phenomenon can be explained by the enhanced reactivity of heptane under higher pressure,

371 which can only be simulated reliably with sufficiently detailed chemical mechanisms such as LU-55.

372 The above numerical simulations demonstrate that the improved LES methedology can capture

373 quantitative differences in the ignition delay and flame LOL due to different ambient densities, in

374 good agreement with Sandia data.

375 Fig.11 presents the ignition delay time over a very wider range of ambient temperatures from

376 850 K to 1300 K under oxygen concentration of 21% and ambient density of 14.8 kg/m^3. It illustrates

377 that increased ambient temperature results in decreased ignition delay time due to fast evaporation

378 and mixture formation, followed by increased chemical reactivity simultaneously. A good agreement

379 between the LES predictions and the Sandia experimental data has been obtained over a wide range

380 of ambient temperatures except at 850 K and 1300 K. At the low ambient temperature of 850 K, the

381 chemical reactivity is low and the combustion temperature is also low, which leads to increased

382 difficulty in accurately determining the ignition delay time in both experiment and simulation. This

383 is the same situation as with the low oxygen concentration shown in Figs. 8 and 9. As for the high

384 ambient temperature of 1300 K, the experimental data shows almost the same ignition delay time

385 under 1200 K and 1300 K, respectively, which is abnormal. The increased discrepancy with the LES

386 prediction under the ambient temperature of 1300 K may be due to an experimental error.

5 Conclusions

In this paper, improved large eddy simulation (LES) with high-order numerical schemes and detailed chemical mechanisms has developed and applied to study liquid fuel spray and turbulent combustion in a constant volume chamber. The third-order MUSCL scheme is employed, which leads to enhanced numerical accuracy. Meanwhile, for combustion simulation, an n-heptane reduced mechanism (58 species, 387 reactions) is implemented with parallel computation using Message-Passing Interface (MPI). The resulting KIVALES-CP code has been validated in various flow/spray/flame configurations and superior performance is demonstrated over the KIVALES base code.

In order to validate the MUSCL numerical scheme, an axisymmetric piston-cylinder engine assembly is used. It is shown that the use of the MUSCL scheme can reduce numerical diffusion and thus obtain better predictions of axial mean velocity at different locations than using the QSOU scheme, as compared with the experiment data. In the diesel spray case, simulation results with QSOU show that eddy structures in the gas phase are suppressed by numerical diffusion. And it overpredicts the vapor length compared with the experiment data, unless very fine grid is used, at a much higher computational cost. In contrast, using the MUSCL scheme with the coarse base grid can give an excellent agreement with the Sandia data. In addition, the results using the MUSCL scheme capture more small eddies and strong vortex regions, even at the Q value of $4.5*10^8$. The MUSCL scheme can capture the same trend as the experiment data for different hydrocarbon fuels with different boiling points and liquid densities. For reacting cases, using parallel computation via MPI can significantly reduce computational time. The improved LES incorporating the MUSCL scheme, subgrid spray models and realistic chemical mechanisms for heptane in KIVALES-CP predicts qualitatively and quantitatively correct results in agreement with experimental under diesel

engine-like conditions, except at some special points where experimental errors are also large. The

flame lift-off length and ignition delay time reduce in response to increase in ambient temperature,

ambient density and oxygen concentration, respectively. In summary, the improved LES

methodology presented in this study has been successful in predicting the velocity distribution,

droplet and vapor phase distribution and combustion characteristics under a very wide range of

conditions.

6 Acknowledgements

Reference

[1]   Rutland, C. Large-eddy simulations for internal combustion engines–a review, International Journal of Engine Research,2011, 12 (5), pp. 421-451.

[2]   Hori, T., Kuge, T., Senda, J.,Fujimoto, H., Large Eddy Simulation of Diesel Spray Combustion with Eddy-Dissipation Model and CIP Method by Use of KIVALES, SAE Paper 2007-01-0247, 2007

[3]   Moureau, V., Barton, I., Angelberger, C.,Poinsot, T. Towards large eddy simulation in internal-combustion engines: simulation of a compressed tumble flow, SAE Paper   2004, 2004-01-1995.

[4]   Thobois, L., Lauvergne, R., Poinsot, T.,Cerfacs, P., Using LES to investigate reacting flow physics in engine design process, 2007-01-0166, 2007

[5]   Bekdemir, C., Somers, L., de Goey, L., Tillou, J.,Angelberger, C. Predicting diesel combustion characteristics with large-eddy simulations including tabulated chemical kinetics, Proceedings of the Combustion Institute,2013, 34 (2), pp. 3067-3074.

[6]   Musculus, M.P., Miles, P.C.,Pickett, L.M. Conceptual models for partially premixed low-temperature diesel combustion, Progress in Energy and Combustion Science,2013, 39 (2), pp. 246-283.

[7]   Taghavifar, H., Taghavifar, H., Mardani, A.,Mohebbi, A. Modeling the impact of in-cylinder combustion

440		parameters of DI engines on soot and NOx emissions at rated EGR levels using ANN approach, Energy
441		Conversion and Management,2014, 87 (0), pp. 1-9.
442	[8]	Imtenan, S., Varman, M., Masjuki, H.H., Kalam, M.A., Sajjad, H., Arbab, M.I.,Rizwanul Fattah, I.M. Impact of
443		low temperature combustion attaining strategies on diesel engine emissions for diesel and biodiesels: A review,
444		Energy Conversion and Management,2014, 80 (0), pp. 329-356.
445	[9]	Jing, W., Roberts, W.L.,Fang, T. Spray combustion of Jet-A and diesel fuels in a constant volume combustion
446		chamber, Energy Conversion and Management,2015, 89 (0), pp. 525-540.
447	[10]	Pickett LM. Engine combustion network, "http://www.sandia.gov/ecn."
448	[11]	Kong, S.-C., Marriott, C.,Reitz, R.D., Modeling and experiments of HCCI engine combustion using detailed
449		chemical kinetics with multidimensional CFD, SAE: 2011-01-1026, 2001
450	[12]	Sone, K.,Menon, S. Effect of subgrid modeling on the in-cylinder unsteady mixing process in a direct injection
451		engine, Journal of Engineering for Gas Turbines and Power-Transactions of the Asme,2003, 125 (2), pp.
452		435-443.
453	[13]	Van Leer, B. Towards the ultimate conservative difference scheme. II. Monotonicity and conservation combined
454		in a second-order scheme, Journal of computational physics,1974, 14 (4), pp. 361-370.
455	[14]	Nordin, N. The KIVA Jumpstation [Online]. Available:
456		http://www.tfd.chalmers.se/~nordin/KJS/.
457	[15]	Bharadwaj, N., Rutland, C.,Chang, S. Large eddy simulation modelling of spray-induced turbulence effects,
458		International Journal of Engine Research,2009, 10 (2), pp. 97-119.
459	[16]	Patterson, M.A.,Reitz, R.D., Modeling the Effects of Fuel Spray Characteristics on Diesel Engine Combustion
460		and Emissions, SAE Paper 980131, 1998
461	[17]	Jonnalagedda, S., Nguyen, T., Zhou, B.,Sobiesiak, A., Numerical Investigation of HCCI Combustion in an IDI
462		Type Diesel Engine Fueled with Isooctane, SAE 2011-01-1181, 2011
463	[18]	Senecal, P., Pomraning, E., Richards, K., Briggs, T., Choi, C., McDavid, R.,Patterson, M. Multi-dimensional
464		modeling of direct-injection diesel spray liquid length and flame lift-off length using CFD and parallel detailed
465		chemistry, SAE transactions,2003, 112 (3), pp. 1331-1351.
466	[19]	Jagus, K.,Jiang, X. Large Eddy Simulation of Diesel Fuel Injection and Mixing in a HSDI Engine, Flow,
467		turbulence and combustion,2011, 87 (2-3), pp. 473-491.
468	[20]	Zhou, L., Xie, M., Jia, M.,Zhou, Q., Influences of subgrid turbulent kinetic energy and turbulent dispersion on
469		the characteristics of fuel spray, SAE 2011-01-1839 2011
470	[21]	Pickett, L.M., Genzale, C.L., Bruneaux, G., Malbec, L.-M., Hermant, L., Christiansen, C.,Schramm, J.
471		Comparison of diesel spray combustion in different high-temperature, high-pressure facilities, SAE Int. J.
472		Engines,2010, 3 (2), pp. 156-181.
473	[22]	Idicheria, C.A.,Pickett, L.M. Effect of EGR on diesel premixed-burn equivalence ratio, Proceedings of the
474		Combustion Institute,2007, 31 (2), pp. 2931-2938.
475	[23]	Morse, A.P., Whitelaw, J.H.,Yianneskis, M.; Imperial College Dept. Mech.: 1978.
476	[24]	Qin, W.J., Xie, M.Z., Jia, M.,Zhou, L. Large eddy simulation of turbulent flows and cyclic variations in internal
477		combustion engine, Journal of Engineering Thermophysics,2011, 32 (1), pp. 268-271.
478	[25]	Chakraborty, P., Balachandar, S.,Adrian, R.J. On the relationships between local vortex identification schemes,
479		Journal of Fluid Mechanics,2005, 535 (1), pp. 189-214.
480	[26]	Myong, K.-J., Suzuki, H., Senda, J.,Fujimoto, H. Evaporation characteristics of multi-component fuel,
481		Fuel,2006, 85 (17), pp. 2632-2639.
482	[27]	Lu, T.,Law, C.K. Linear time reduction of large kinetic mechanisms with directed relation graph:n-Heptane and
483		iso-octane, Combustion and Flame,2006, 144 (1), pp. 24-36.
484	[28]	Curran, H., Gaffuri, P., Pitz, W.J.,Westbrook, C.K. A comprehensive modeling study of n-heptane oxidation,
485		Combustion and flame,1998, 114 (1-2), pp. 149-177.
486	[29]	Liu, S., Hewson, J.C., Chen, J.H.,Pitsch, H. Effects of strain rate on high-pressure nonpremixed n-heptane

487   autoignition in counterflow, Combustion and flame,2004, 137 (3), pp. 320-339.

488   [30]   Liu, Y.-D., Jia, M., Xie, M.-Z.,Pang, B. Enhancement on a Skeletal Kinetic Model for Primary Reference Fuel

489   Oxidation by Using a Semidecoupling Methodology, Energy & Fuels,2012, 26 (12), pp. 7069-7083.

490   [31]   Yoo, C.S., Lu, T., Chen, J.H.,Law, C.K. Direct numerical simulations of ignition of a lean   n-heptane/air

491   mixture with temperature inhomogeneities at constant volume: Parametric study, Combustion and Flame,2011,

492   158 (9), pp. 1727-1741.

493   [32]   Patel, A.,Kong, S.-C., "Development and validation of a reduced reaction mechanism for HCCI engine

494   simulations,"   SAE paper 2004-01-0558, 2004.

495   [33]   Ra, Y.,Reitz, R.D. A reduced chemical kinetic model for IC engine combustion simulations with primary

496   reference fuels, Combustion and Flame,2008, 155 (4), pp. 713-738.

497   [34]   Tsurushima, T. A new skeletal PRF kinetic model for HCCI combustion, Proceedings of the Combustion

498   Institute,2009, 32 (2), pp. 2835-2841.

499

500

501

502

503

504

505

506

507

508

509

510

511

512

513

514   Figures

515   Fig. 1   Axisymmetric piston-cylinder assembly of Morse et al.

516   Fig. 2   Distribution of axial mean velocity with radial distance from axial at crank angle of ATDC 36º and ATDC

517   144º

518   Fig.3   Measured and predicted penetration length and fuel mass fraction at 1.5 ms for liquid and vapor phase using

519   MUSCL and QSOU under base grid(about 800,000 cells) and dense grid (about 6 million cells) for Case 1

520   Fig. 4   The evolution of vortex field with injection time at 1.5ms after start of injection for MUSCL and QSOU

521   under base grid (case 1)

522   Fig.5   Comparison of predicted results using LES and experiment image by mie-scattered light and shadowgraph

523   at the end of injection of 1.82ms for case 2

524   Fig.6   Change in liquid phase length obtained through simulation using MUSCL and QSOU and experiment at

525   different fuel density for case 2.

526   Fig.7   Measured and predicted temperature and OH contours under different EGR at 2.0ms ASOI for Case 3

527   （ ambient density=14.8 kg/m^3, ambient initial temperature=1000 K). Dashed white line is flame lift-off

528   length.

529   Fig.8   Measured and predicted ignition delay and flame lift-off length at different EGR for Case 3 (ambient

530   density=14.8kg/m^3, ambient initial temperature=900 K and 1000K)

531   Fig.9   Measured and predicted ignition delay time under different oxygen concentration (ambient density=30.0

532   kg/m^3, ambient initial temperature=1000K).

533   Fig.10   Influence of ambient density on temperature distribution under oxygen concentration of 15% and ambient

534   temperature of 1000 K

535   Fig.11   Measured and predicted ignition delay time at different ambient temperature under oxygen concentration

536   of 21% (ambient density=14.8 kg/m^3)

537

538

539

540

541

542

543

544

545

546 # Tables

547 <div align="center">Table 1 Experimental conditions</div>

Case	Fuel	Hole diameter （mm）	Injection duration （ms）	Injection pressure （MPa）	Fuel mass （mg）	fuel temperature （K）	ambient gas oxygen	Ambient density （kg/m^3 ）	Ambient temperature （K）	Ref.
Case 1	C12H26	0.09	1.54	150	3.5	363	0% (non-reacting)	22.8	900	[21]
Case 2	C8H18 C12H26 C16H34	0.2	1.82	72	12	368	0% (non-reacting)	15.0	700	[26]

| Cas e 3 | C7H16 | 0.1 | 6.8 | 150 | 17.8 | 373 | 10%~21% (reacting) | 14.8, 30. | 850-1300 | [22] |

548

549

Table 2 Comparison of computation time using different numerical schemes

	Base grid	Dense grid
QSOU	7 CPU hours	72 CPU hours
MUSCL	8 CPU hours	80 CPU hours

550

551

Table 3 The ignition delay time at two oxygen concentrations (21% and 12%) using seven reduced n-heptane

mechanisms.

	Ignition delay time predicted by different reduced chemical mechanisms (Unit: ms)							
	LIU-SL	LIU-YD	LU-88	Patel	Ra	TS	Lu-55	Exp.data
Species numbers	44[29]	37[30]	88[31]	29[32]	41[33]	35[34]	55[31]	N/A
21% O_2	0.65	0.60	0.57	0.61	1.0	0.64	0.57	0.53
12% O_2	1.2	1.48	0.90	1.3	2.7	1.3	0.92	0.95

554

555

556

557

558

559

560

561

562
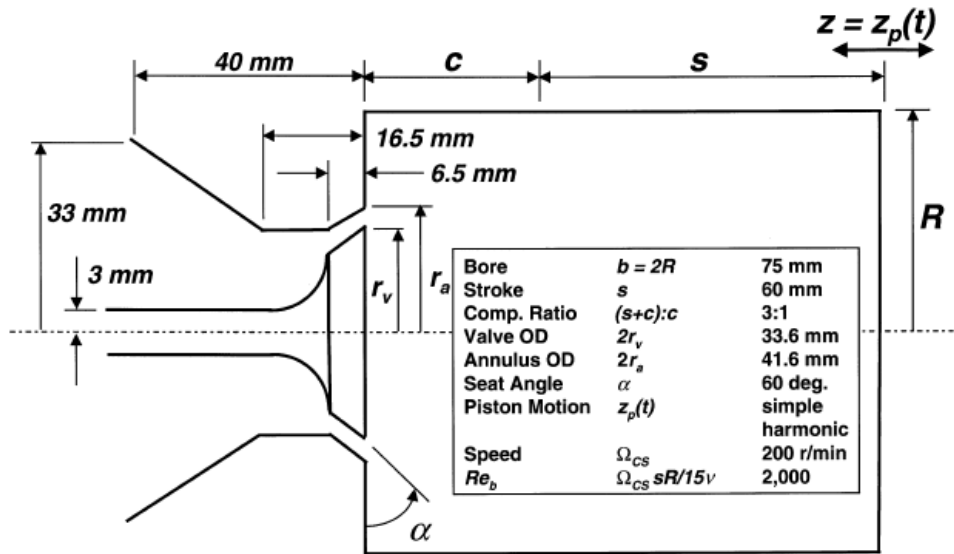
563
564   Fig. 1   Schematic of the axisymmetric piston-cylinder assembly of Morse et al. [23]
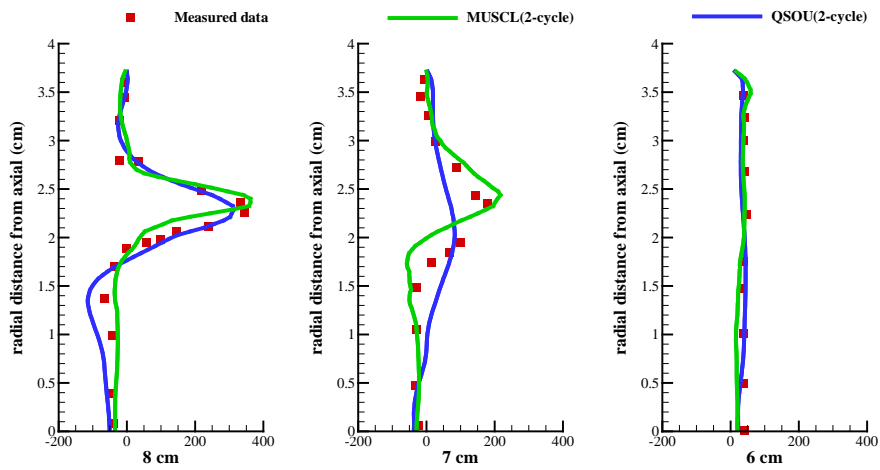
565

566

567

568

569

570

571

572

573

574

575

576

577　　　　　　　　　　　　　　　　Axial mean velocity (cm/s)

578　　　　　　　　　　　　　　　　　2 a)　　ATDC 36º
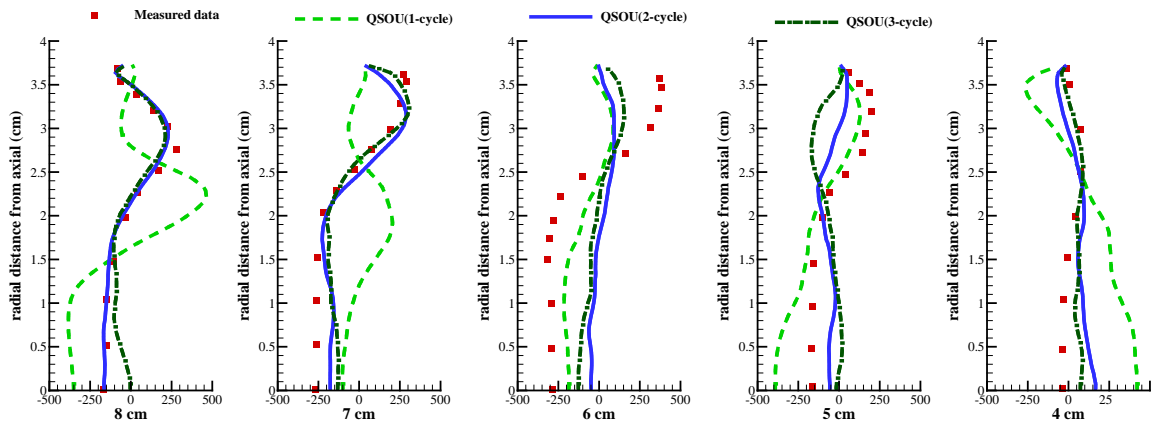
579

580　　　　　　　　　　　　2 b) Predictions by QSOU Scheme ATDC 144º
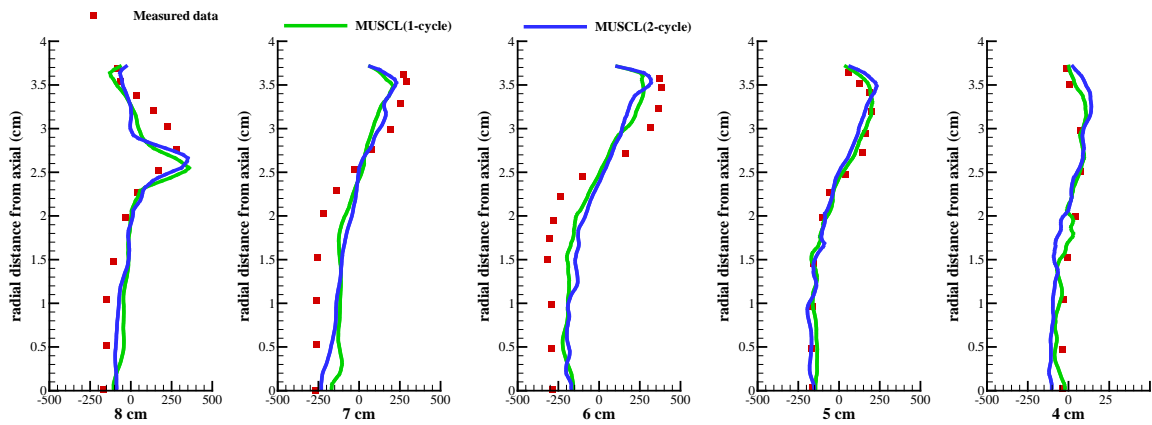
581

582　　　　　　　　　　　　2 c) Predictions by MUSCL Scheme ATDC 144º

583　　　　　　　　　　　　　　　　Axial mean velocity(cm/s)

584　　　　　　Fig.2　　Radial distribution of axial mean velocity at crank angle of ATDC 36º and ATDC 144º

585
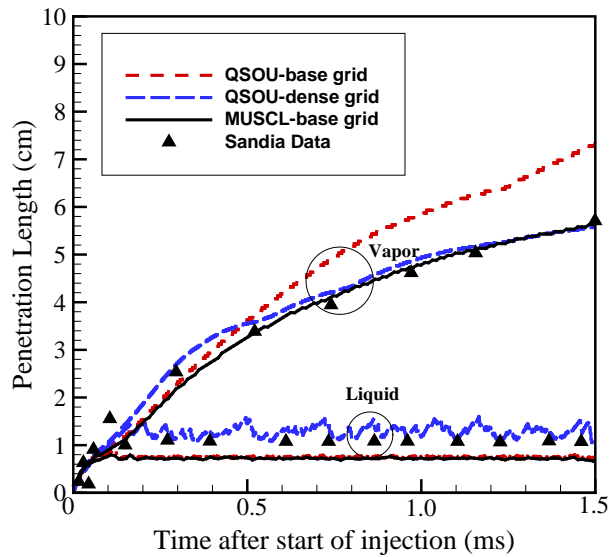
586

587   3 a)   Penetration length variation with time after fuel injection

588
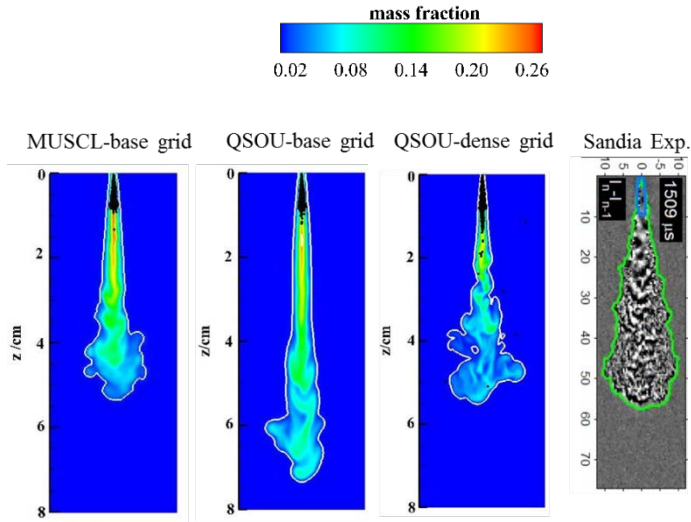
3b) Liquid and vapor mass fraction distribution

591   Fig. 3   Measured and predicted penetration length and fuel mass fraction at 1.5 ms for liquid and vapor phase

592   using MUSCL and QSOU on base grid (about 800,000 cells) and dense grid (about 6 million cells) for Case 1

593

594

595

596

597

598

599

600
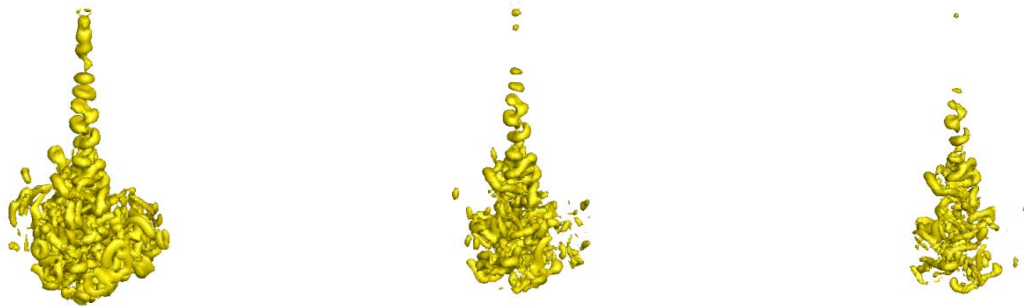
MUSCL with base grid

QSOU with base grid

Q=1.5*10^7 Q=1.5*10^8 Q=4.5*10^8

601   Fig.4 The vortex field at 1.5ms after start of injection for MUSCL and QSOU schemes on the base grid (Case 1)

602

603

604

605

606

607

608

609

610

611

612

613

614

615

616

617

618

Mass Fraction
0.02 0.08 0.14 0.20 0.26 0.32

LES   Exp.
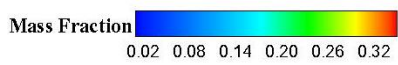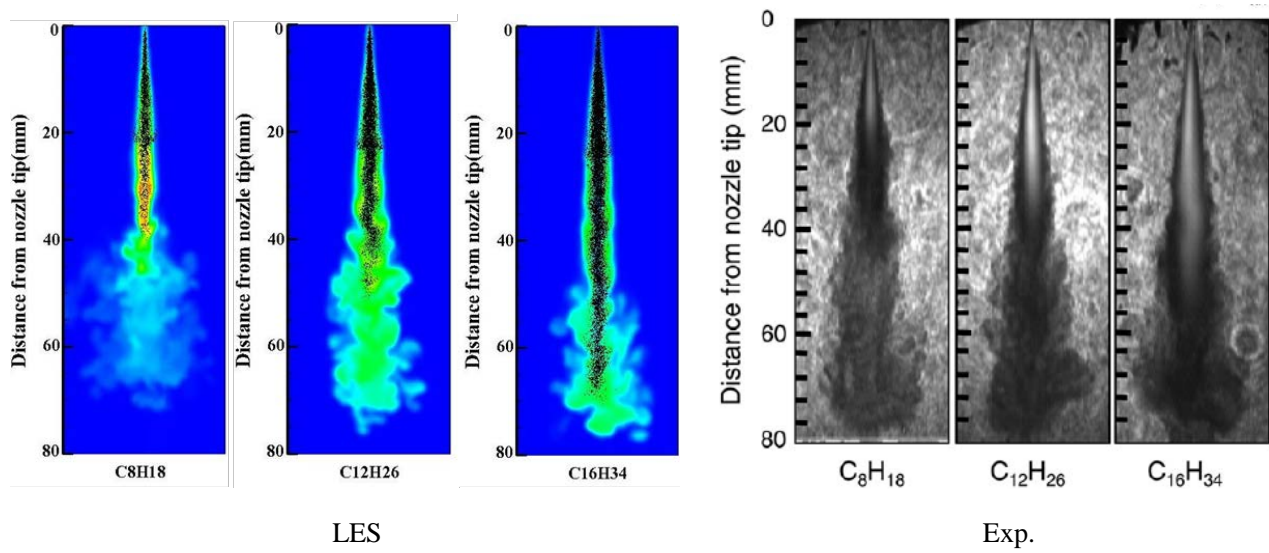
619   Fig.5 Comparison of predicted results using LES and experiment images by Mie-scattered light and shadowgraph

620   at the end of injection of 1.82ms for Case 2 (Ref.[20])

621

622

623

624

625

626

627

628

629

630

631

632

633

634

635

636

637

638
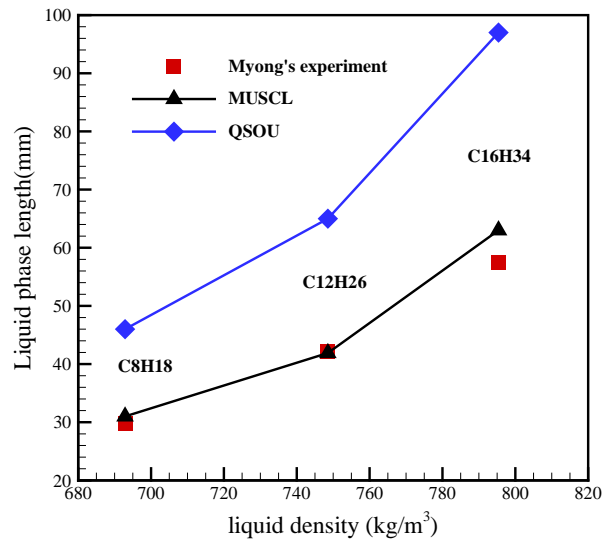
Fig. 6 Liquid phase length obtained through simulation using MUSCL and QSOU and experiment at different fuel densities for Case 2.
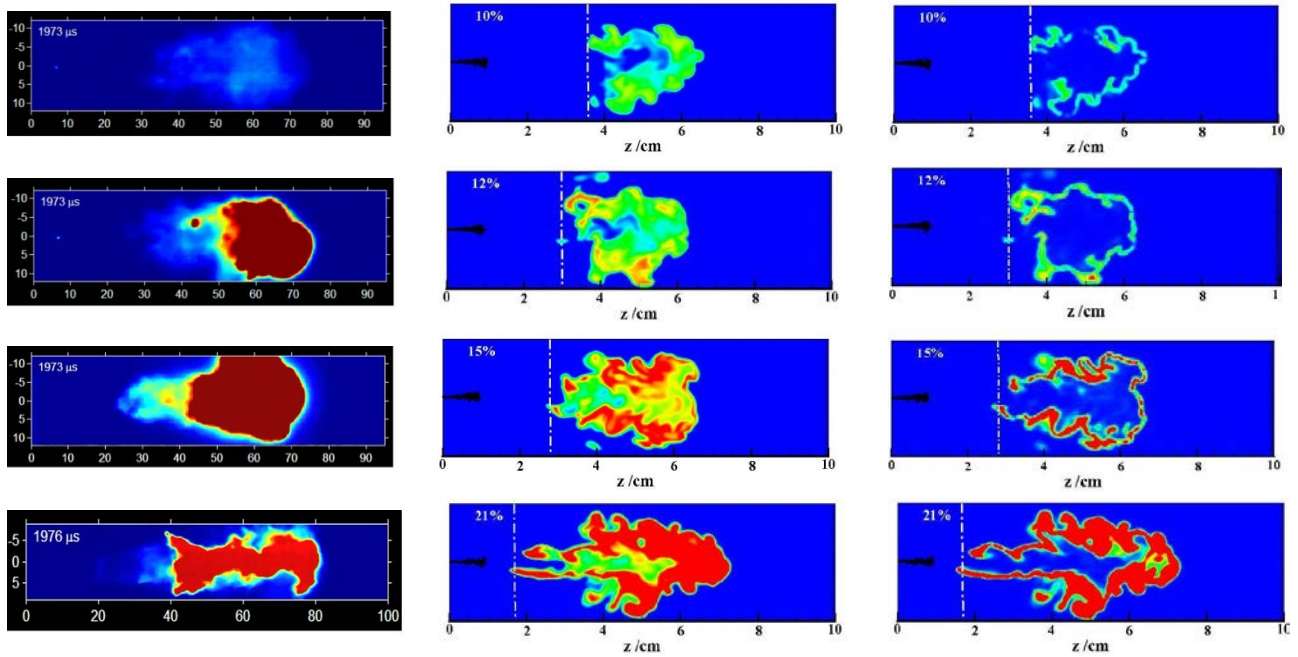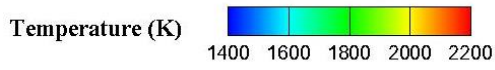
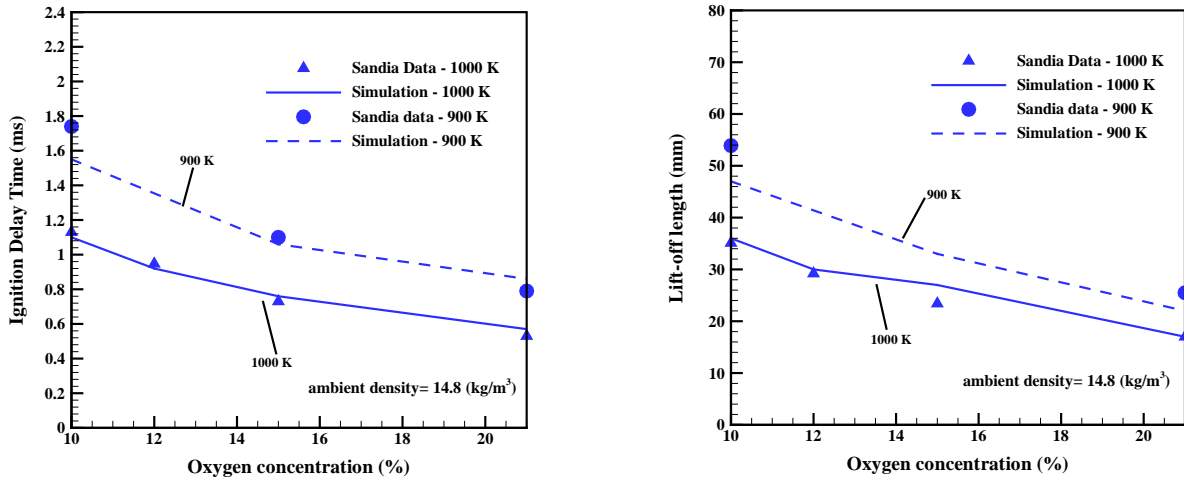| Sandia chemiluminescence image | Temperature | OH radical |

662   Fig.7   Measured and predicted temperature and OH contours under different EGR at 2.0 ms ASOI for Case 3

663   (ambient density14.8 kg/m^3, ambient initial temperature1000 K). Dashed white line indicates the flame lift-off

664   length.

665

666

667

668

669

670

671

672

673

674

675

676

677

678

679

680

681   Fig.8   Measured and predicted ignition delay and flame lift-off length at different EGR for Case 3 (ambient

682   density=14.8kg/m^3, ambient initial temperature=900 K and 1000K)

683

684

685

686

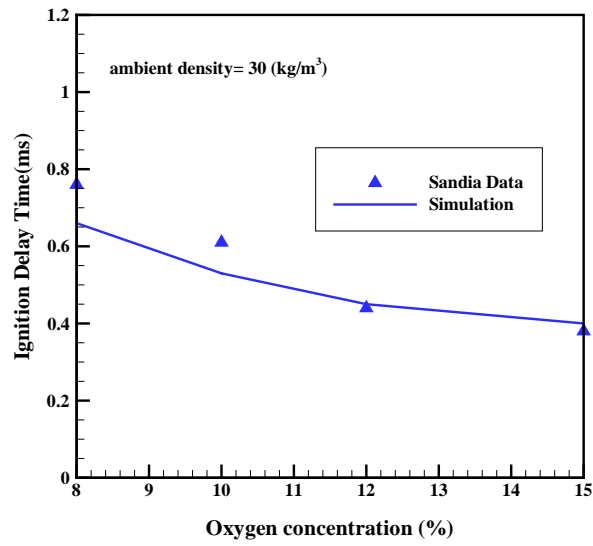687

688

689

690

691

692

693

694

695

696

697

698

699

700

701

702

Fig. 9   Measured and predicted ignition delay time under different oxygen concentrations (ambient density 30.0

kg/m^3, ambient initial temperature 1000K).

725

726

10 a) ambient density=14.8 kg/m³   10 b) ambient density=30.0 kg/m³
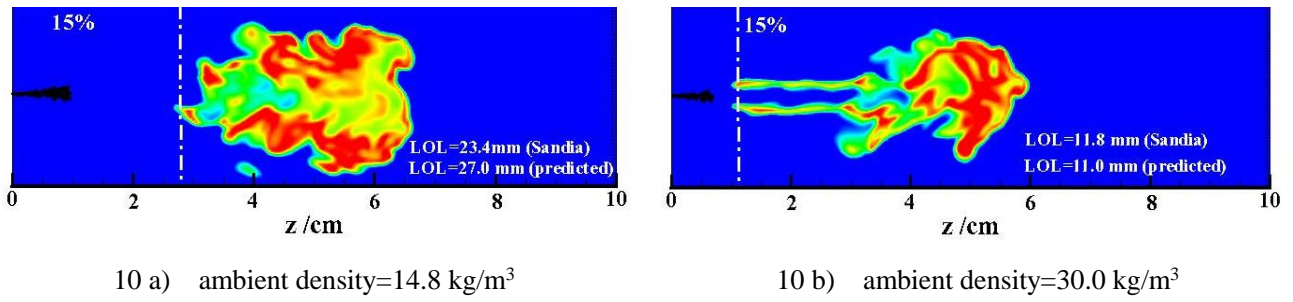
727 Fig.10 Influence of ambient density on temperature distribution under oxygen concentration of 15% and ambient

728 temperature of 1000 K

729

730

731

732

733

734

735

736

737

738

739

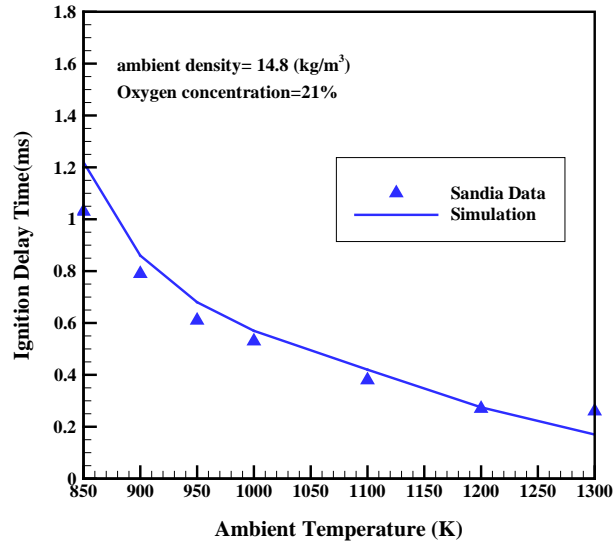740

741

742

743

744

745

746

747

748

749

750

751

ambient density= 14.8 (kg/m³)
Oxygen concentration=21%

▲   Sandia Data
—— Simulation

752

753   Fig.11   Measured and predicted ignition delay time at different ambient temperatures under oxygen concentration

754   of 21% (ambient density=14.8 kg/m³)

755

756

757

758

759

760

761